Science Essence Journal Vol. 41 No. 2 (2025) | 141-167

Research Article

In Vitro Screening of Anti-Viral and Virucidal Effects Against SARS-CoV-2 by Phenylamino-Phenoxy-Quinoline Derivatives: An Integrative Computational Approach

Suwicha Patnin[1], Arthit Makarasen[1*], Akanitt Jittmittraphap[2], Pornsawan Leaungwutiwong[2], Pongsit Vijitphan[1], Apisara Baicharoen[1], Natchaphon Ngueanngam[3] and Supanna Techasakul[1*]

Received: 20 May 2025
Revised: 26 June 2025
Accepted: 1 July 2025

ABSTRACT

This study investigated the binding interactions between three groups of 2,4-disubstituted phenylamino-phenoxyquinoline derivatives **1-3(a-d)** and four readily available drugs (ritonavir, ensitrelvir, nirmatrelvir, and paxlovid) with severe acute respiratory syndrome coronavirus 2 (SARS-CoV-2) using cytotoxicity, virucidal activity testing, molecular docking, and molecular dynamic methods. Between the concentration range of 500 to 31.25 μg/mL, **1-3(a-d)** demonstrated that none of the investigated substances had any harmful effects on Vero E6 cells. The virucidal activity testing demonstrated that ritonavir, ensitrelvir, nirmatrelvir, paxlovid, and **3c** had log reduction values ranging from 2.99 to 3.50 when treated with concentrations between 62.5 to 125 μg/mL. Ritonavir and **3c** had exceptional log reduction values that surpassed those of the other substances examined. **3c** exhibited the highest log reduction value when compared to the other 2,4-disubstituted quinoline derivatives evaluated at the same concentration. The molecular docking approach revealed that all analyzed compounds interacted with the active site of the SARS-CoV-2 main protease (M^{pro}) through hydrogen bonds and π-sulfur interactions. Furthermore, molecular dynamics simulations, combined with binding free energy calculations using MM-PBSA and MM-GBSA techniques, demonstrated the binding free energy of M^{pro}-ensitrelvir and M^{pro}-**3c** was greater than that of M^{pro}-**1a**. To validate our computational results, we conducted M^{pro} inhibitor screening assay. The analysis was confirmed that compound **3c** exhibits strong inhibitory activity (IC_{50} = 2.71 μM), consistent with our virucidal testing and computational approaches. The results emphasize the potential of 2,4-disubstituted quinoline derivatives as promising candidates for inhibiting SARS-CoV-2. This provides crucial insights for developing effective antiviral drugs.

Keywords: SARS-CoV-2, Quinoline, Virucidal Activity, Molecular docking, Molecular Dynamic

[1] Department of Chemistry, Laboratory of Organic Synthesis, Chulabhorn Research Institute, Bangkok 10210, Thailand
[2] Department of Microbiology and Immunology, Faculty of Tropical Medicine, Mahidol University, Bangkok 10400, Thailand
[3] Department of Chemistry, Faculty of Science, Srinakharinwirot University, Bangkok 10110, Thailand
*Corresponding author, email: arthit@cri.or.th, supanna@cri.or.th

Introduction

The severe acute respiratory syndrome coronavirus 2 (SARS-CoV-2) has caused the COVID-19 pandemic, which has had a major global impact, with over 774 million illnesses and 7 million deaths reported as of February 2024 [1]. Beyond its significant public health issues, the ongoing crisis has spread throughout society and economies around the world, necessitating an urgent search for viable therapeutic approaches. For the development of optimal treatment strategies, it is critical to understand the behavior of SARS-CoV-2, closely related to the coronaviruses responsible for the 2014 Middle East respiratory syndrome (MERS) epidemic and the 2003 severe acute respiratory syndrome (SARS-CoV) outbreak [2, 3]. A comprehensive understanding of the viral cycle, from cellular attachment to proliferation, is essential for finding possible treatment targets. A new and interesting idea is to stop the main viral replication enzymes, such as main protease (M^{pro}), RNA-dependent RNA polymerase (RdRp), and papain-like protease (PLpro), a crucial enzyme involved in virus replication that converts viral polyproteins into essential functional proteins required for virus assembly [4-6]. The amino acid residues of M^{pro}, particularly HIS41 and CYS145, play an essential role in inhibiting the catalytic triad mechanism of the proteolytic cleavage process, halting virus replication, and limiting intracellular infection. M^{pro} is a dimeric protein with three subdomains that each comprise 306 amino acid residues. This protein exhibits an active site situated in a cleft between domain I (residues 8−99) and domain II (residues 100−183) [7-9]. Currently, the development of inhibitors, particularly for the main protease (M^{pro}), is being actively explored. M^{pro} inhibitors contribute significantly to limiting viral replication by cleaving viral polyproteins into essential functional components required for virus assembly. Several types of M^{pro} inhibitors have been utilized for an application in emergency circumstances, such as the SARS-CoV-2 pandemic. These M^{pro} inhibitor medicaments include telaprevir, boceprevir, lopinavir, ritonavir, N3, GC376, ensitrelvir, nirmatrelvir (PF-07321332), and Paxlovid. To describe the background of these drugs, the first protease inhibitors, telaprevir and boceprevir, were developed in order to treat Hepatitis C Virus (HCV). They inhibit the NS3/4A serine protease, an enzyme highly important in viral replication. These have been significant in the use of protease inhibitors, which were effective in reducing viral replication and enhancing the treatment outcomes [10, 11]. Later, protease inhibitors, such as lopinavir and ritonavir, developed against human immunodeficiency virus (HIV), found other clinical uses. Traditionally, these drugs inhibit the action of an enzyme, HIV protease, which is important for producing viral polyproteins. Ritonavir acts like a "booster" by increasing the blood concentration of lopinavir, enhancing its effectiveness. This strategy was tried eventually in early SARS-CoV-2 trials. As expected, the results were similar to the treatment of HIV disease. Hence these trials show how existing drugs can be modified to address diseases that have been recently discovered [12, 13]. After that, GC376 and N3 were studied for the research and development of a novel anti-viral medication against SARS-CoV-2. GC376 was developed at an earlier stage for animal infections, especially the feline coronavirus responsible for feline infectious peritonitis (FIP) in cats. This drug leads to the fact that protease inhibitors can suppress the activity of M^{pro}, related to the mechanism that is described above in SARS-CoV-2. The investigation into GC376 has explored avenues for the development of drugs for SARS-

CoV-2 treatment in humans. On the contrary, N3 is one of those molecules that were designed and studied in particular for inhibiting M^{pro} directly in biochemical experiments, introducing new ideas in the field of drug design against key viral enzymes [14-16]. Ensitrelvir is a non-covalent, non-peptidic SARS-CoV-2 M^{pro} inhibitor developed by Shionogi & Co. and prevents viral replication in host cells. Early trials showed that ensitrelvir greatly reduced the viral load and sped up the recovery time of COVID-19 patients, hence it is considered one of the most promising therapeutic candidates under current clinical evaluation [17, 18]. Nirmatrelvir (PF-07321332) was developed by Pfizer specifically against COVID-19. This compound acts by mechanisms of a potent protease inhibitor with very high specificity against the M^{pro} of SARS-CoV-2, attaching to the active site of the enzyme and impeding viral replication. The development was based on information from previous protease inhibitors and has resulted in the design of a more specific and suitable drug for treatment in COVID-19 [19, 20]. Lastly, Paxlovid is one of the well-known antivirals developed by Pfizer. It synergistically combines nirmatrelvir, a potent M^{pro} inhibitor, with ritonavir, a pharmacokinetic enhancer. This combination principally works by inhibiting the liver enzyme CYP3A4, responsible for the metabolism of nirmatrelvir. The action time and its bioavailability of nirmatrelvir in an organism should be prolonged. Clinical trials showed that Paxlovid is highly effective, it significantly reduced the rate of hospitalization and death among people who experienced mild-to-moderate SARS-CoV-2 symptoms when the medication was timely administered starting from the beginning of symptom appearance [21-23].

Building upon our previous investigation in 2022, which comprised designing and synthesizing 2,4-disubstituted quinoline derivatives utilizing a molecular hybridization technique and integrating HIV-1 RT drug pharmacophores, we discovered that these compounds have remarkable anti-HIV-1 RT potency [24, 25]. These compounds displayed less cytotoxicity in normal cells and excellent affinity to interact with transporter proteins [26]. Our previous research revealed their potential for inhibiting HIV-1 RT, which fascinated our interest in assessing their efficacy against SARS-CoV-2. Given that disubstituted quinoline derivatives are nitrogen-containing molecules with nitrile side chains, they are similar to the currently available SARS-CoV-2 medical treatments. In a previous study, we thoroughly investigated the binding interactions of 2-phenylamino-4-phenoxyquinoline, 6-phenylamino-4-phenoxyquinoline derivatives, and six commercially available drugs (hydroxychloroquine, ritonavir, remdesivir, ensitrelvir, N3, and nirmatrelvir) with SARS-CoV-2's main protease (M^{pro}). Our study, which employed molecular docking and the ONIOM approach, revealed important information regarding the binding affinity and interaction energy of these substances with M^{pro}. Our results exhibited that 2-phenylamino-4-phenoxyquinoline has a higher binding affinity than 6-phenylamino-4-phenoxyquinoline, as evidenced by calculations of binding free energy and interaction energy [27].

Recently, in-silico studies in computational chemistry techniques, such as molecular docking, molecular dynamics simulations, and binding free energy calculations (Molecular Mechanics/Generalized Born Surface Area (MM-GBSA) and Molecular Mechanics/Poisson-Boltzmann Surface Area (MM-PBSA), have become significant in studying the inhibitory effects of biological compounds on SARS-

CoV-2. These computational approaches provide valuable insights into the binding affinity and mechanism of potential inhibitors, suggesting in the design and optimization of antiviral agents [28].

The present investigation comprehensively investigates molecules obtained through molecular design and synthesis, with a specific focus on 2,4-disubstituted quinoline derivatives divided into three groups: compounds **1(a-d)**, compounds **2(a-d)**, and compounds **3(a-d)**. The main objective of this study is to evaluate quinoline derivatives and commercial pharmaceutical drugs utilizing a variety of approaches such as cytotoxicity, virucidal activity testing, molecular docking, and molecular dynamics. This comprehensive study aims to significantly contribute to our understanding of the antiviral characteristics of these quinoline derivatives, potentially laying the framework for their utility in combating SARS-CoV-2.

Materials and Methods

Virus Preparation

The SARS-CoV-2 virus was isolated from nasopharyngeal swabs of a confirmed COVID-19 patient in Thailand and authenticated by the Virology Laboratory 10/34 at the Department of Microbiology and Immunology, Faculty of Tropical Medicine, Mahidol University. Whole-genome sequencing of the viral RNA confirmed the Delta B.1.617.2 variant. Vero E6 cells (CRL-1586) were cultured in Minimum Essential Media (MEM) supplemented with 10% heat-inactivated FCS, 1% glutamine, and 1% penicillin-streptomycin. The virus was propagated in Vero E6 cells using MEM supplemented with 2% fetal calf serum (FCS) and 1% penicillin-streptomycin. A high-titer viral stock was obtained after incubating the virus-infected Vero E6 cells at 37 °C in a 5% CO_2 humidified incubator for 72 hours. Viral titer was determined by 50% tissue culture infectious dose ($TCID_{50}$) [29]. The virus stock was serially diluted 10-fold in quadruplicate in 96-well microtiter plates containing Vero E6 cells in Roswell Park Memorial Institute (RPMI) 1640 medium. The switch from MEM to RPMI is likely to maintain Vero E6 cell health during the calculation of the viral titer. Vero E6 cells thrive in RPMI-1640 medium [30]. After incubation at 37°C in a 5% CO_2-humidified incubator for 72 hours, the $TCID_{50}$ was determined by observing the visible cytopathic effect (CPE). The Reed-Muench method is used to statistically calculate the dilution at which 50% of the wells would be infected (the $TCID_{50}$) [31]. Results were expressed as $TCID_{50/mL}$. All experiments involving the live SARS-CoV-2 virus were strictly conducted using biosafety level 3 (BSL3) facilities at Mahidol University.

Cytotoxicity Assay

The cytotoxicity assay aimed to assess the potential adverse effects of synthesized compounds on host cells. Synthesized compounds were initially prepared as stock solutions in 0.5% dimethyl sulfoxide (DMSO). The compound was tested at concentrations ranging from 1000 to 7.8125 μg/mL, using two-fold serial dilutions in culture media. The chemical structures of antiviral agents and quinoline derivatives 1-3(a-d) are depicted in Figure 1. The negative control consisted of compound-free MEM, while 0.5% DMSO served as the vehicle control. Each test compound was evaluated through 3

independent experiments, with quadruplicate per trial. Vero E6 cells were seeded into 96-well plates ($2x10^4$ cells/well) and incubated at 37 °C for 24 hours until confluent monolayers formed. Following the removal of culture supernatant, the cell monolayers were washed twice with sterile phosphate-buffered saline (PBS). Various concentrations of synthesized compounds were applied to the cells, while compound-free MEM served as the negative control. The treated cells were further cultivated for 48 hours. After treatment, cell viability was assessed using an MTT assay by incubating the cells with MEM containing 0.5 mg/mL of MTT for another 2 hours in a CO_2 incubator. Then, the media were removed, and DMSO (200 μL/well) was added to lyse the cells and solubilize formazan crystals. Absorbance at 570 nm was measured using a microplate reader, and the percentage of cell viability was calculated relative to the negative control [32].

Virucidal Activity Testing

The virucidal activity testing was performed on Vero E6 cells that were cultivated in MEM supplemented with 10% heat-inactivated fetal calf serum (FCS) for cell culture maintenance and 2% FCS during virus propagation. In addition, the medium was composed of 1% glutamine and 1% penicillin-streptomycin [33]. SARS-CoV-2 was propagated and titrated in Vero E6 cells using the 50% Tissue Culture Infectious Dose Assay ($TCID_{50}$) [34]. The assessment of virucidal activity was conducted in accordance with the parameters specified in the American Society for Testing and Materials (ASTM) standard E1053-20 [35]. The synthesized compounds were dissolved and diluted to the desired concentrations in MEM. In order to evaluate the ability of the compounds to eradicate the SARS-CoV-2 virus, a concentrated viral solution containing $2x10^5$ $TCID_{50/mL}$ was incubated with the diluted test compounds and left to incubate for an exposure time of 6 hours. Subsequently, the mixture was neutralized and filtered. The filtrate was diluted in a series of 10-fold dilutions and then applied into 96-well plates containing Vero E6 cells. Each test compound was evaluated through 3 independent experiments, with quadruplicate per trial. The plates were subsequently placed in a CO_2 incubator and kept at a temperature of 37 °C for a duration of 72 hours. Following the incubation period, the wells were examined for cytopathic effects that indicated the presence of infected cells. Additionally, the Reed–Muench method was employed to determine the quantity of residual viruses [31]. A 0.21% sodium hypochlorite solution served as the positive control. The effectiveness of the test compound was measured by comparing it to the control, expressed in terms of log reduction and percentage efficacy. To be classified as virucidal, a compound needed to achieve a minimum 3-log reduction or 99.9% effectiveness.

Ligand and Protein Structure Preparation

This study investigates the binding interactions between M^{pro} and several ligands, including three medical treatments present in commerce (ritonavir, ensitrelvir, and nirmatrelvir) as well as twelve synthesized quinoline derivatives. The ligands were prepared by employing Gaussian 16 to build their structures, followed by fully optimizing compounds using density functional theory (DFT) at the B3LYP/6-31G (d, p) level [36, 37]. The crystallographic structure of the M^{pro} enzyme bound to

nirmatrelvir were obtained from the Protein Data Bank (PDB ID: 7VH8) [38]. Subsequently, the synthesized ligands were subjected to molecular docking and molecular dynamics methods to examine the binding interactions with the M^{pro} structure.

Molecular Docking

In order to commence the molecular docking simulations, the M^{pro} structure underwent preparation by eliminating the nirmatrelvir and water molecules, subsequently adding hydrogen atoms. The ligand-protein interactions were simulated using AutoDock 4.2 software [39], which assumes that the protein remains rigid during the docking process. The Lamarckian Genetic Algorithm (LGA) was utilized for the molecular docking calculations. A population size of 150 individuals was employed, and the maximum number of genetic algorithm runs was set to 150. The dimensions of the grid box were specified as 80 x 80 x 80 Å, with a spacing of 0.375 Å. The M^{pro} grid was centered at positions -18.099, 17.279, and -25.630 Å. Further analysis was conducted on compounds that achieved the highest docking scores as a result of the docking simulations. The chosen compounds were visually examined using Accelrys Discovery Studio Client 4.0 software.

Molecular dynamic

The GROMACS software (v2022.3), developed by the University of Groningen in the Netherlands, was utilized to perform molecular dynamics (MD) simulations [40]. The protein and ligand topologies were generated using the AmberTools 22 program [41]. The ligand acquired the relevant RESP charge using the B3LYP/6-31G (d) method, and the general AMBER force field 2 (GAFF2) was used to derive the ligand's force field parameters [42]. The ligands with the lowest binding energy chosen for the MD simulation investigation were **1a**, **3c**, and ensitrelvir. In order to analyze the stability and conformational changes of the M^{pro}-ensitrelvir, M^{pro}-**1a**, and M^{pro}-**3c** complexes through the use of MD simulations, the simulations were carried out with the AMBER14SB force field [43]. The complexes were placed in the center of an octahedral box using the TIP3P water model [44], with a spacing distance of 10 Å from the edge of the box. Notably, the protonation status of ionizable residues was evaluated by utilizing a pH of 7.4 with the assistance of the PDB2PQR webserver. Sodium ions and chloride ions were added to the solvent systems in order to neutralize the charges and achieve a physiological concentration of 0.15 M. The AMBER topology and coordinates of the complexes were generated using the Python script ParmEd, which converts them into GROMACS topologies. The steepest descent approach was employed to minimize energy, with a tolerance value of 10 kJ/mol·nm. Subsequently, the complete system was equilibrated for 1000 ps. A molecular dynamics (MD) simulation was conducted for a total time of 300 nanoseconds (ns) while maintaining a constant temperature of 310.15 Kelvin and a pressure of 1 bar. Furthermore, the findings of the molecular dynamics (MD) simulation were examined using the Visual Molecular Dynamics (VMD) program [45]. Moreover, we employed the simulation trajectory to identify the state of least structural energy for the complexes using

the free energy landscape (FEL). Hence, we used a simulation trajectory from the time after the global energy minimum state to calculate the binding free energy of the complexes.

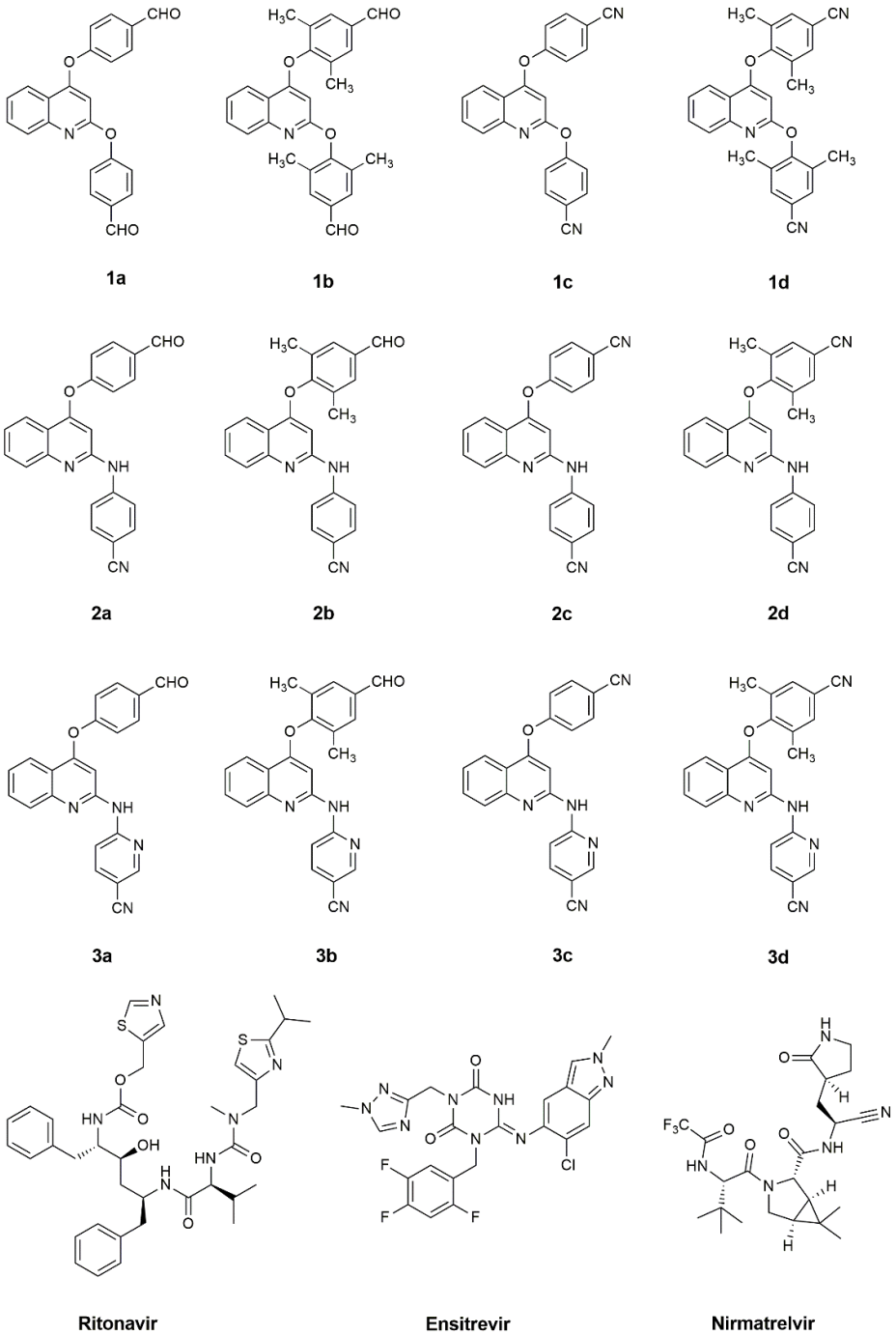

Figure 1 The structures of the current medicaments along with the quinoline derivatives **1(a-d)**, **2(a-d)**, and **3(a-d)**.

Binding free energy calculation

In order to evaluate the binding affinities of the M^{pro}-ensitrelvir, M^{pro}-**1a**, and M^{pro}-**3c** complexes, we utilized established computational approaches, specifically the Molecular Mechanics/Poisson-Boltzmann Surface Area (MM-PBSA) and Molecular Mechanics/Generalized Born Surface Area (MM-GBSA) [46]. These methods are highly effective techniques commonly used in the analysis of protein-ligand interactions and drug design [47, 48]. The binding free energy and per-residue decomposition free energy were calculated using 1000 frames obtained from the region of the Gibbs free energy landscape corresponding to the global energy lowest state. The calculations were performed to evaluate the binding affinity of the complexes using the MM-(GB)PBSA method. We utilized the modified Generalized Born (GB) model 2 and Poisson-Boltzmann (PB) model 2 in the MM-GBSA and MM-PBSA models, respectively. In addition, the solvation energy of the complexes was determined using the GB and PB models, employing an implicit solvent dielectric constant of 78.5 and 80, respectively. The dielectric constant parameters for the solute were uniformly assigned a value of 3, while the ionic strength was adjusted to 0.15 M in order to mimic physiological conditions. The computations utilized suitable methods and implemented the interaction entropy (IE) approach, with a solvent probe radius of 1.4 Å. This approach incorporates the energy from molecular mechanics, the solvation-free energy calculated using the Poisson-Boltzmann equation, and the nonpolar contribution computed using the solvent-accessible surface area (SASA) model. The evaluation of all binding free energy outcomes was performed using the gmx_MMPBSA_ana software, which is a component of the gmx_MMPBSA package. Furthermore, these binding free energy estimates yield significant insights into the strength of the interactions between the ligands (ensitrelvir, **1a**, and **3c**) and M^{pro}, providing precise quantitative assessments of their binding affinities. This information is crucial for the rational development and improvement of new medication candidates.

SARS-CoV-2 Main Protease Inhibitor Screening Assay

The inhibition of SARS-CoV-2 main protease (M^{pro}) by the selected compounds (**1a** and **3c**) was evaluated using the Cayman Chemical SARS-CoV-2 Main Protease Inhibitor Screening Assay Kit (Item No. 701960) [49]. SARS-CoV-2 main protease assay was performed in a 96-well microplate, with a final volume of 100 μL per well. Background wells received 70 μL of assay buffer (supplemented with DTT) plus 10 μL of solvent. Wells designated for 100% enzyme activity were prepared by adding 50 μL of assay buffer, 20 μL of diluted recombinant enzyme, and 10 μL of solvent. For inhibitor testing, 50 μL of assay buffer, 20 μL of enzyme, and 10 μL of inhibitor solution were added in triplicate. The selected compounds namely, **1a** and **3c**, were evaluated at various concentrations (50, 25, 12.5, 6.25, 3.125, 1.56, 0.78, and 0.39 μM). After dispensing the reagents, the plate was incubated at room temperature for 30 minutes. The reaction was initiated by adding 20 μL of substrate (diluted in assay buffer), followed by sealing the plate and incubating for 2 hours at room temperature in the dark. Fluorescence was measured using a microplate reader with an excitation wavelength of 340 nm and an emission wavelength of 490 nm. Data were corrected by subtracting the background signal, and percent

inhibition was calculated using the equation: % Inhibition = [(Corrected Control - Corrected Sample) / Corrected Control] × 100. The IC_{50} values of **1a** and **3c** were determined from the resulting dose-response curve.

Results and Discussion

Cytotoxicity Assay

The cytotoxicity assay evaluated the effects of substances consisting of 2,4-disubstituted quinoline derivatives and four commercially accessible medications (ritonavir, ensitrelvir, nirmatrelvir, and paxlovid) on Vero E6 cells, utilizing the MTT assay. Among the compounds **1-3(a-d)**, the cell viability exceeded 80% at concentrations below 500 μg/mL, except for **1a** and **1c** may be attributed to their structural features, specifically the presence of electron- and **1c**. These two compounds showed slightly lower cell viability, ranging from 70% to 86% when Vero E6 cells were treated at the concentration of 125 to 500 μg/mL. This slightly reduced viability with **1a** withdrawing groups at specific positions on the quinoline ring. These structural elements could influence cellular uptake and potentially lead to mild off-target effects. However, importantly, the viability of **1a** and **1c** remains above the acceptable threshold of 70% for cytotoxicity studies, indicating these compounds are suitable for further investigation.

The commercially available drugs, ritonavir and nirmatrelvir, demonstrated cell viability of over 70% at the concentrations below 125 and 500 μg/mL, respectively. However, ensitrelvir and paxlovid exhibited cell survival above 80% at the concentrations below 250 and 500 μg/mL, respectively. The results are presented in Figure 2 and documented in Table S1 (see also Supplementary Materials). The study concluded that the 2,4-disubstituted quinoline derivatives, nirmatralvir, and paxlovid were not causing any toxicity to Vero E6 cells at concentrations ranging from 31.25 to 500 μg/mL. Additionally, ritonavir and ensitrelvir did not have any harmful effects on Vero E6 cells at concentrations below 125 and 250 μg/mL, respectively. To assess cell viability when exposed to the tested compounds, a minimum survival rate of 70% of the cells is required [50]. The concentration that demonstrated cell viability at that rate will be utilized to determine virucidal activity against SARS-CoV-2.

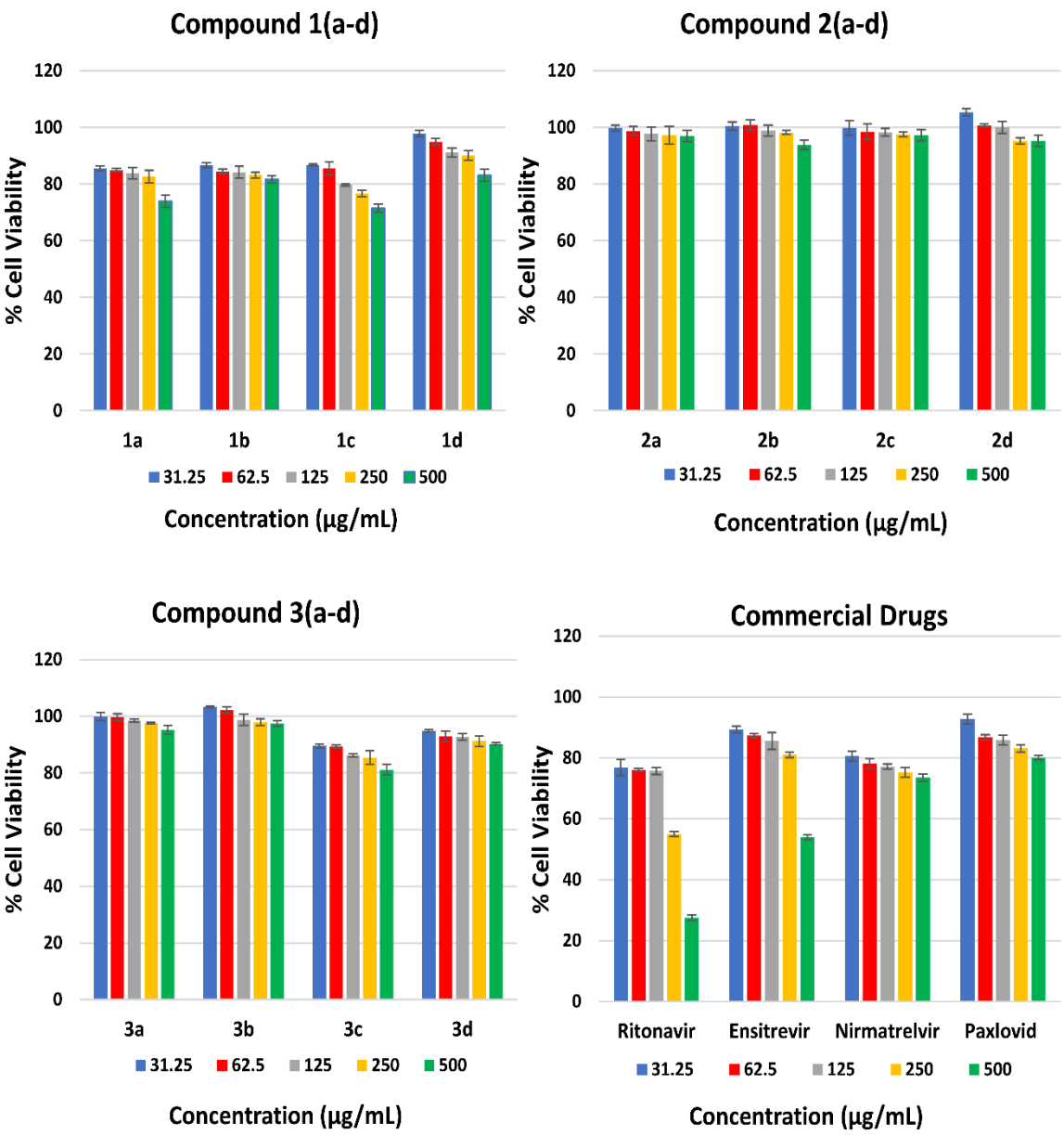

Figure 2 The percentage of cell viability in response to different concentrations of quinoline derivatives **1-3(a-d)** and four commercially available medicines (ritonavir, ensitrelvir, nirmatrelvir, and paxlovid).

Virucidal activity testing

The evaluation of the antiviral effectiveness of 2,4-disubstituted quinoline derivatives and conventional medications adhered carefully to the guidelines set by the American Society for Testing and Materials (ASTM) standard E1053–20 [37]. This standard provides a comprehensive framework for evaluating virucidal activity against enveloped viruses, including coronaviruses. It ensures reproducible testing conditions. The objective of the study was to analyze the results of experiments into log reduction values for SARS-CoV-2. This would provide a numerical measure of the decrease in the number of viable microbes accomplished through disinfection [51]. All of the tested 2,4-disubstituted quinoline derivatives, **1-3(a-d)**, showed significant log reduction values higher than 2.68, indicating

over 99.77% efficacy across the concentration range of 31.25 to 500 μg/mL, as illustrated in Figure 3. These results were obtained through an investigation that provided compelling results. In comparison to the other 2,4-disubstituted quinoline derivatives, **3c** had the highest log reduction value when compared with the same concentration that was evaluated. According to the cytotoxicity assay described above, the commercially available medications, namely ritonavir and ensitrelvir, demonstrated cell viability of less than 70% on Vero E6 cells when treated at concentrations higher than 250 and 500 μg/mL, respectively. In order to minimize cell toxicity and decrease interference with the experimental investigation for SARS-CoV-2 inhibition, the virucidal study utilized concentrations ranging from 7.82 to 125 μg/mL for ritonavir and 15.63 to 250 μg/mL for ensitrelvir, respectively.

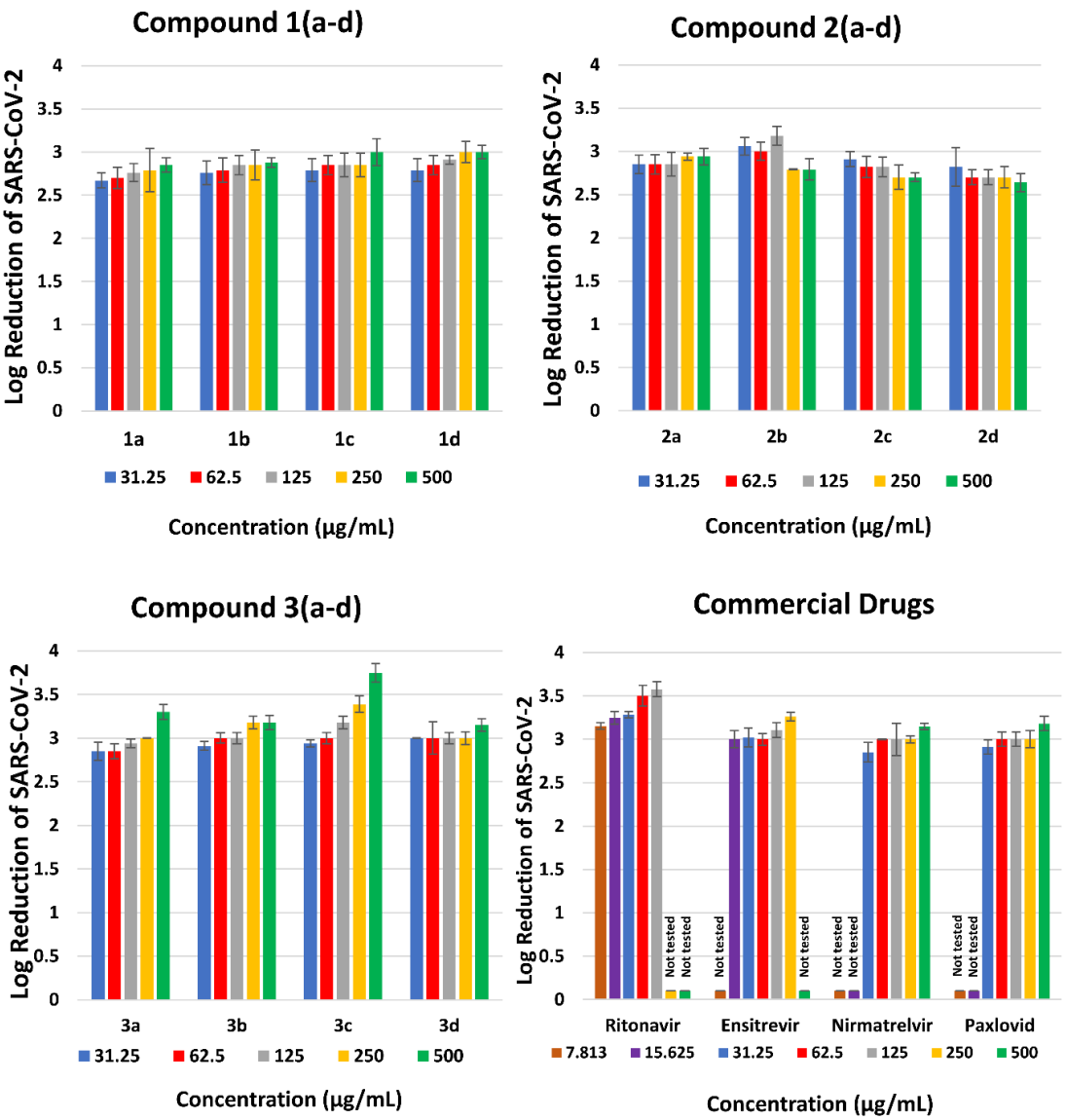

Figure 3 The log reduction of SARS-CoV-2 in response to different concentrations of quinoline derivatives **1-3(a-d)** and four commercially available medications (ritonavir, ensitrelvir, nirmatrelvir, and paxlovid).

The study found that, across concentrations higher than 31.25 μg/mL, the virucidal activity outcome for commercially accessible medications (ritonavir, ensitrelvir, nirmatrelvir, and paxlovid) illustrated log reduction values higher than 2.83, indicating impressive effectiveness over 99.85%, as shown in Figure 3. The additional digital data is available and is presented in Table S1 (see also Supplementary Materials). Additionally, the results demonstrated that ritonavir, Ensitrelvir, nirmatrelvir, paxlovid, and **3c** exhibited log reduction values that varied from 2.99 to 3.50 when treated at concentrations ranging from 62.5 to 250 μg/mL. It is remarkable that ritonavir and **3c** displayed outstanding log reduction values that were higher than those of the other investigated compounds. Comparative analysis revealed that compound **3c** exhibited comparable activity to ensitrelvir across all concentrations tested (31.25-500 μg/mL). At 125 μg/mL, **3c** showed a log reduction value of 3.16, similar to ensitrelvir (3.12) and superior to nirmatrelvir (3.05). Statistical analysis using one-way ANOVA confirmed no significant difference between **3c** and ritonavir ($p > 0.05$). Hence, the efficacy of 2,4-disubstituted quinoline derivatives in inhibiting the SARS-CoV-2 virus was successfully determined. Especially, **3c** revealed similar effectiveness to the current pharmaceutical medications used for COVID-19 treatment, discovering the promising possibilities for valuable novel antiviral medications.

Molecular Docking

Using molecular docking, we studied the binding interactions of currently available medications (ritonavir, ensitrelvir, and nirmatrelvir) and quinoline derivatives **1-3(a-d)** with the SARS-CoV-2 main protease (M^{pro}). In the molecular docking investigation, ritonavir and nirmatrelvir were utilized as representations of paxlovid because paxlovid is manufactured by combining the two of those substances. The objective of this study was to identify the most significant binding modes for drug development. All selected ligands effectively bound to the hydrophobic cavity within the M^{pro} binding pocket (Figure 4). The overlay analysis revealed a consistent binding region shared among the analyzed compounds. The compounds interacted with specific amino acid residues of M^{pro}, including HIS41, MET49, TYR54, PHE140, LEU141, ASN142, SER144, CYS145, HIS163, HIS164, MET165, GLU166, HIS172, GLN189, THR190, ALA191, and GLN192. These interactions, which include hydrogen bonds and hydrophobic interactions, are crucial for inhibiting M^{pro} activity [52-54]. Quinoline derivatives **1-3(a-d)** demonstrated conventional hydrogen bonds with the amino acid residues of M^{pro}, including HIS41, SER144, CYS145, HIS163, MET165, GLU166, THR190, and GLN192. Carbon-hydrogen bonds were discovered among PRO52, LEU141, SER144, MET165, HIS172, GLN189, ALA191, and GLN192. π-sulfur interactions are associated with CYS145 and MET165. The π-π stacking interaction involved HIS41. The three available medications demonstrated that conventional hydrogen bonding interactions with M^{pro} involved HIS41, TYR54, PHE140, ASN142, SER144, CYS145, HIS163, HIS164, GLU166, GLN189, THR190, and GLN192. Carbon-hydrogen bonds appeared with MET165, GLU166, ARG188, and GLN189. π-sulfur interactions are involved with MET49 and MET165. The π-π stacking interaction affected HIS41. In the literature review, it was found that HIS41 and CYS145 are key residues in the catalytic site of the enzyme [7-9], whereas GLU166 is engaged in the substrate-binding

site and dimer structure of M^{pro} [55]. Figures S1-S4 (Supplementary Materials) show visual representations of various ligand-M^{pro} interactions. The binding energy values between the ligands and M^{pro} ranged from -8.56 to -10.61 kcal/mol (Table 1). Nirmatrelvir had the lowest binding energy of -10.61 kcal/mol, followed by **3c** (-10.25 kcal/mol) and **1a** (-10.02 kcal/mol).

Ensitrelvir and ritonavir exhibited binding energy values of -9.62 and -8.56 kcal/mol, respectively. Furthermore, molecular docking investigations revealed that nirmatrelvir, ensitrelvir, **1a**, and **3c** exhibit potential binding interactions with M^{pro}, particularly with the catalytic site and substrate-binding area. These research findings prompted the selection of ensitrelvir, **1a**, and **3c** for further molecular dynamics (MD) simulations. Specifically, compounds **1a** and **3c** were chosen due to their superior binding energy values (-10.02 and -10.25 kcal/mol, respectively), and their favorable interaction profiles with critical M^{pro} residues, including the catalytic dyad HIS41 and CYS145, as well as GLU166 and GLN192. Their binding poses demonstrated multiple hydrogen bonds and π-interactions that closely mimic those of known inhibitors, suggesting enhanced potential as M^{pro}-targeting agents. Ensitrelvir, being a non-covalent, non-peptidic inhibitor of SARS-CoV-2 M^{pro}, aligns well with the binding interactions observed for the selected compounds [17-18]. Our goal is to investigate the stability of the M^{pro}-ligand complexes, establish their interactions, and compute the binding free energy to acquire a better understanding of their potential as antiviral agents against SARS-CoV-2.

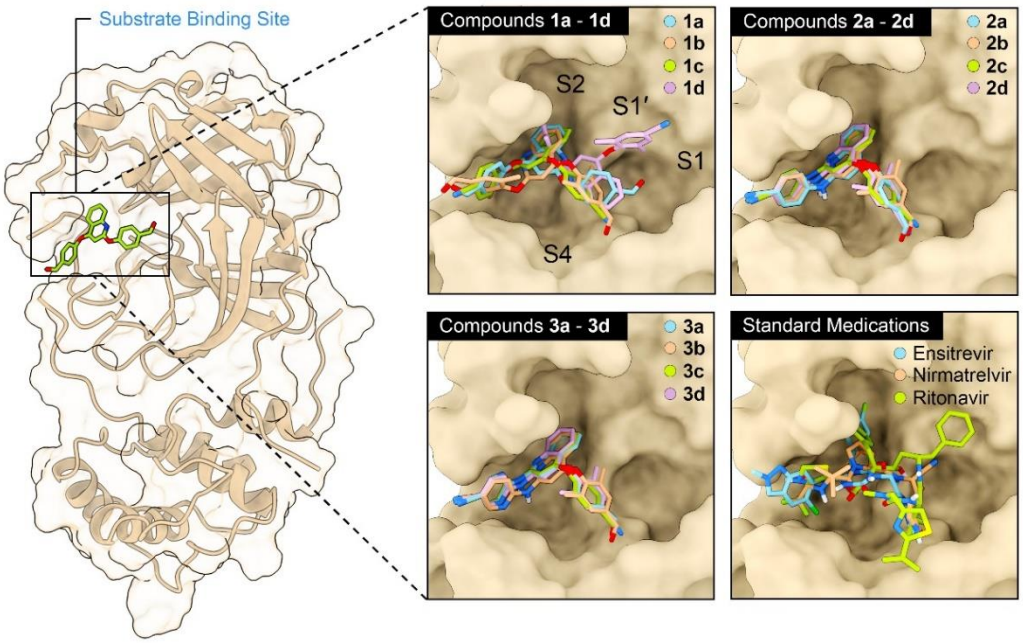

Figure 4 The overlaying of conformations for current medications, namely ritonavir, ensitrelvir, and nirmatrelvir, alongside the investigated compounds **1(a-d)**, **2(a-d)**, and **3(a-d)** within the binding pocket of M^{pro}, as determined through molecular docking.

Table 1 Binding interaction between ligands with M^{pro} in 3.0 Å.

Ligands	Binding energy (kcal/mol)	Hydrogen bond		π-Sulfur	π-π Stacking
		H-bond[a]	H-bond[b]		
1a	-10.02	CYS145 GLU166 GLN192	LEU141 SER144	MET165	HIS41
1b	-9.98	HIS163 GLN192	LEU141 HIS172	CYS145	HIS41
1c	-9.94	SER144 HIS163	-	CYS145 MET165	-
1d	-9.94	HIS41 GLU166	PRO52 MET165	-	-
2a	-9.81	HIS163	HIS172 ALA191	-	-
2b	-9.98	-	LEU141 ALA191	MET165	-
2c	-9.96	SER144 HIS163 MET165	-	CYS145 MET165	-
2d	-9.19	HIS163 MET165	-	CYS145 MET165	-
3a	-9.68	HIS163 MET165 THR190	LEU141GLN189	CYS145 MET165	-
3b	-9.78	HIS163	LEU141 HIS172 GLN192	CYS145	-
3c	-10.25	SER144 HIS163 MET165 THR190	GLN189	CYS145 MET165	-
3d	-9.98	SER144 MET165	GLN192	CYS145 MET165	-
Ritonavir	-8.56	ASN142 CYS145 HIS164	MET165 ARG188	MET49	HIS41
Ensitrelvir	-9.62	HIS41 TYR54 CYS145 GLU166 GLN189	PHE140 GLU166 MET165	MET165	HIS41
Nirmatrelvir	-10.61	HIS41 PHE140 SER144 CYS145 HIS163 HIS164 GLU166 THR190 GLN192	MET165 GLN189	-	-

[a] Conventional hydrogen bond. [b] Carbon hydrogen bond.

Molecular Dynamic Simulations

The utilization of molecular dynamics (MD) simulations was done with the objective of determining the stability of the binding that occurs between ligands and the target protein. These simulations made it possible to conduct an in-depth investigation of the stability and conformational changes that occurred within a solvent environment [56, 57]. The root mean square deviation (RMSD) of the protein backbone, the root mean square fluctuation (RMSF), and the radius of gyration (Rg) were among the major characteristics that were examined during a 300 ns MD simulation in order to evaluate the binding stability of ensitrelvir, **1a**, and **3c** within the M^{pro} binding site. The RMSD served as a significant indicator of binding stability, providing insights into the equilibrium state of the complex in the simulated system. RMSD calculations were carried out for M^{pro}-free, M^{pro}-ensitrelvir, M^{pro}-**1a**, and M^{pro}-**3c**, and the results are depicted in Figure 5A. During the molecular dynamics simulation that continued for 300 ns, ensitrelvir, **1a**, and **3c** achieved the ability to form an intact bond with the M^{pro} binding site. The RMSD data demonstrated that the M^{pro}-ensitrelvir, M^{pro}-**1a**, and M^{pro}-**3c** complexes had lower RMSD values when compared to the M^{pro}-free complex. Notably, the RMSD of M^{pro}-**3c** was significantly lower than that of M^{pro}-**1a** and M^{pro}-free. The presence of ligands in the active site of M^{pro} has an effect on the structural stability of the protein. Interestingly, binding **3c** with M^{pro} resulted in less fluctuation compared to unbound M^{pro}. This suggests that the simulations of the binding process reached a state of equilibrium and stability. It was also found that M^{pro}-**1a** was less stable than M^{pro}-ensitrelvir and M^{pro}-**3c** due to fluctuations that occurred throughout the simulation operations. This was discovered when the RMSD fluctuations of the three complexes were compared.

The RMSF analysis provided an expansive understanding of the fluctuations that occurred in the amino acid residues throughout the MD simulation. Figure 5B displays the results of the RMSF calculations for M^{pro} and its complexes with ensitrelvir, **1a**, and **3c**. The RMSF plots suggest that stable interactions between the ligand and the protein are characterized by reduced fluctuations of the residues in the backbone atoms. On the other hand, higher fluctuations indicate that the protein structure seems more flexible, which may indicate that conformational changes are occurring. The results definitely demonstrate that M^{pro}-ensitrelvir, M^{pro}-**1a**, and M^{pro}-**3c** had lower RMSF values than M^{pro}-free at HIS41, PHE140, LEU141, ASN142, GLY143, SER144, CYS145, HIS163, MET165, GLU166, LEU167, HIS172, THR190, and GLN192. This indicates that three compounds were able to form stable complexes, with the active site being the location where the highest level of structural stability was expressed. Moreover, the RMSF values of M^{pro}-ensitrelvir and M^{pro}-**3c** at HIS41, MET49, LEU141, ASN142, GLY143, SER144, CYS145, HIS163, MET165, GLU166, HIS172, THR190, and GLN192 are lower than those of M^{pro}-**1a**. According to the results shown in Table 1, these observations are in accordance with the binding interactions that were predicted by molecular docking studies. Because of these findings, it appears that ensitrelvir and **3c** bind to the M^{pro} active site with more stability than **1a**, which leads to a reduction in the number of fluctuations in the residues and an enhancement in the structural stability of the protein-ligand complex, respectively.

Furthermore, the Rg value measured the degree of compactness of the protein structure over the simulation period of time. Within the Rg plot, the protein's fluctuations display a decrease in comparison to the protein-free state, suggesting a higher level of compactness and structural stability for the protein. Figure 5C illustrates the radius of gyration (Rg) for M^{pro} and its complexes with ensitrelvir, **1a**, and **3c**. We can observe that the Rg values for each of the M^{pro} complexes with M^{pro}-ensitrelvir, **1a**, and **3c** are lower than those of M^{pro}-free. This indicates that the binding of three ligands, namely, ensitrelvir, **1a**, and **3c**, promotes a more tightly packed conformation of the protein, potentially leading to enhanced stability of the complexes. Therefore, the MD simulation results for the complex between M^{pro}-ensitrelvir, M^{pro}-**1a**, and M^{pro}-**3c** suggest that the decreased RMSD, RMSF, and Rg values indicate that the conformations of M^{pro}-ensitrelvir and M^{pro}-**3c** are more compact and stable during the binding interaction process compared to M^{pro}-**1a**.

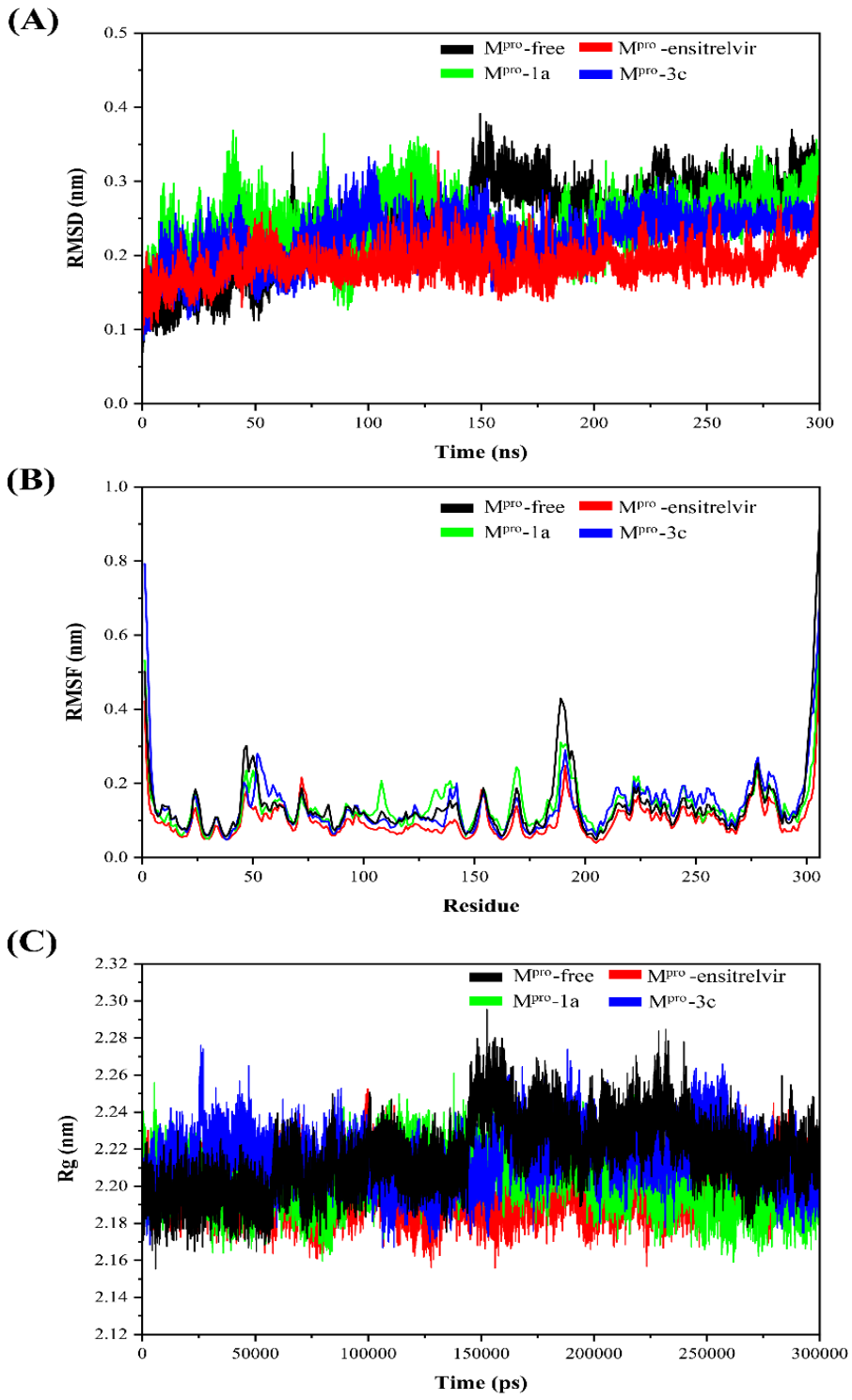

Figure 5 The analyses of MD simulations. (A) RMSD of protein backbone of M^{pro}-free, M^{pro}- ensitrelvir, M^{pro}-**1a**, and M^{pro}-**3c**. (B) RMSF of protein backbone of M^{pro}-free, M^{pro}-ensitrelvir, M^{pro}-**1a**, and M^{pro}-**3c**. (C) Rg graphs of M^{pro}-free, M^{pro}-ensitrelvir, M^{pro}-**1a**, and M^{pro}-**3c**.

Binding Free Energy Calculations

We investigated the structural minimum state in order to ensure that the complexes maintained their structural stability throughout the simulation duration. A better understanding of the thermodynamic aspects of the behavior of molecules and biomolecules can be achieved through the utilization of the free energy landscape (FEL) and principal component analysis (PCA). The FEL provides information regarding the state of the protein-ligand complex with the lowest energy minimum, considering both the energy function and time dimensions [58]. The PCA analysis was calculated using the trajectory of all atoms of protein structure [59]. The utilization of two-dimensional and three-dimensional color maps reveals the FEL (Free Energy Landscape) of M^{pro}- ensitrelvir, M^{pro}-**1a**, and M^{pro}-**3c**, as present in Figures S5A, S5B, and S5C, respectively (see also Supplementary Materials). The state with the lowest energy minimum, which is indicative of the protein-ligand complex associated with the structural stability, is represented by the color purple in the FEL, which indicates the structural stability of the complexes. Subsequently, the structures of the complexes were extracted and analyzed during these time intervals. The results identified the time intervals of global minimal stability observed during the periods of 286-298 ns, 121-135 ns, and 137-153 ns for the M^{pro}-ensitrelvir, M^{pro}-**1a**, and M^{pro}-**3c** complexes, respectively. Therefore, these time intervals were utilized for calculating the binding free energy of those complexes using the molecular mechanics with generalized Born and surface area (MM-GBSA) and molecular mechanics Poisson-Boltzmann surface area (MM-PBSA) approaches [60, 61].

The MM-GBSA and MM-PBSA methods were utilized in order to determine the relative binding free energies between the ligands (ensitrelvir, **1a**, **3c**) and M^{pro}. This was accomplished by considering a variety of energy components, including van der Waals interactions, electrostatic interactions, solvation energies, and entropy contributions. Table 2 provides an overview of the values of the binding free energy that were calculated for the complexes of ensitrelvir, **1a**, and **3c** associated with M^{pro}. The results indicate that the binding free energy demonstrates consistent patterns between the MM-GBSA and MM-PBSA models for all three complexes.

The MM-GBSA model determined the binding free energies ($\Delta G_{Binding/GB}$) for the complexes of ensitrelvir, **1a**, and **3c** with M^{pro} to be -40.16±4.81 kcal/mol, -30.51±2.56 kcal/mol, and -34.32±3.14 kcal/mol, respectively. Upon analyzing the MM-PBSA model, it was discovered that the binding free energies ($\Delta G_{Binding/PB}$) for the ensitrelvir, **1a**, and **3c** complexes with M^{pro} were -38.05±4.70 kcal/mol, -28.47±2.45 kcal/mol, and -32.51±2.86 kcal/mol, respectively. The van der Waals and electrostatic interactions for M^{pro}-**1a** and M^{pro}-**3c** were lower than those for M^{pro}- ensitrelvir in both the MM-GBSA and MM-PBSA models. The binding free energy for each compound had a beneficial impact from van der Waals interactions. As compounds **1a** and **3c** have lower molecular sizes and fewer side chains compared to ensitrelvir, the van der Waals force among the compounds will decrease.

Table 2 Binding energies and individual component energy values obtained from the MM-GBSA and MM-PBSA calculation of M^{pro}-ensitrelvir, M^{pro}-**1a** and M^{pro}-**3c** complexes.

Energetic terms (kcal/mol)	1a	3c	Ensitrelvir
ΔE_{vdw}	-37.99±2.56	-40.06±2.94	-50.50±3.59
ΔE_{ele}	-2.24±2.56	-3.49±0.93	-8.57±1.58
$\Delta G_{polar/GB}$	7.44±0.87	7.57±0.14	14.78±1.29
$\Delta G_{non-polar/GB}$	-4.61±0.28	-4.88±0.44	-5.76±0.33
$\Delta G_{polar/PB}$	8.20±0.86	8.19±1.02	15.62±1.57
$\Delta G_{non-polar/PB}$	-3.34±0.13	-3.69±0.20	-4.50±0.29
$-T\Delta S$	6.90±0.14	6.54±0.13	9.89±0.13
$\Delta G_{bind/GB}$	-30.51±2.56	-34.32±3.14	-40.16±4.81
$\Delta G_{bind/PB}$	-28.47±2.45	-32.51±2.86	-38.05±4.70
ΔE_{vdw}	-37.99±2.56	-40.06±2.94	-50.50±3.59
ΔE_{ele}	-2.24±2.56	-3.49±0.93	-8.57±1.58

ΔE_{vdw} = van der Waals energy, ΔE_{elec} = electrostatic energy, $\Delta G_{polar/GB}$ = The polar solvation free energy obtained from the generalized Born method, $\Delta G_{non-polar/}$GB = Nonpolar solvation free energy obtained from the generalized Born method, $\Delta G_{polar/PB}$ = The polar solvation free energy obtained from the Poisson-Boltzmann method, $\Delta G_{non-polar/PB}$ = Nonpolar solvation energy obtained from the Poisson-Boltzmann method, $-T\Delta S$ = Interaction entropy, $\Delta G_{Binding/GB}$ = Binding free energy (kcal/mol) from the generalized Born method, $\Delta G_{Binding/PB}$ = Binding free energy (kcal/mol) from the Poisson-Boltzmann method.

Additionally, the electrostatic force of M^{pro}-**1a** and M^{pro}-**3c** was found to be lower than that of M^{pro}-ensitrelvir. This can be attributed to the presence of more electronegative atoms in ensitrelvir, which allows for stronger electrostatic interactions, especially hydrogen bonding. Overall, the binding free energies obtained from the MM-GBSA and MM-PBSA models demonstrate comparable tendencies. It should be emphasized that the calculated binding energy tendencies of these complexes indicate that the binding interaction of M^{pro}-**3c** is stronger than that of M^{pro}-**1a** but lower than that of M^{pro}-ensitrelvir. This is in accordance with the stability of the complexes as determined by MD simulations and the binding energy derived from molecular docking. Furthermore, MM-PBSA and MM-GBSA calculations were utilized in order to conduct an analysis of the per-residue energy decomposition that occurred between the ligands (ensitrelvir, **1a**, and **3c**) and M^{pro}, as depicted in Figure 6. The amino acids, namely HIS41, MET49, PHE140, LEU141, ASN142, GLY143, SER144, CYS145, HIS163, HIS164, MET165, GLU166, LEU167, ASP187, ARG188, GLN189, THR190, and GLN192 were identified as crucial amino acids that were involved in these interactions at the protein-ligand complex. The interactions between these residues and the ligands ensitrelvir, 1a, and 3c were essential in stabilizing

their binding at the M^{pro} active site. Especially HIS41 and CYS145, as the catalytic dyad in the M^{pro} active site, exhibited strong binding interactions with three complexes. According to this study, HIS41 and CYS145 are pivotal in stabilizing ligand binding within the active site, underscoring their significance as key targets in inhibitor design. Notably, GLU166 in the ensitrelvir-M^{pro} complex (Figure 6A) and ASP187 in the 3c-M^{pro} complex (Figure 6C) showed the highest energy contributions in MM-PBSA analysis. GLU166, located in the substrate-binding site, plays a key role in ligand stabilization and M^{pro} dimer formation, while ASP187 likely contributes to ligand anchoring and orientation, highlighting distinct interaction features of ensitrelvir and **3c** [17-18]. The results showed that hydrogen bonding and hydrophobic interactions primarily influenced the binding ability of these compounds. Nevertheless, the crucial amino acids acquired by MD simulation differed from those obtained from molecular docking as described above. The reason for the flexibility of the protein-ligand complex in molecular dynamics (MD) simulations, as opposed to the rigidity observed in molecular docking, is that MD simulations allow the atoms to move freely under physiological settings, enabling the complex to explore a more favorable form. The binding interactions of ensitrelvir and **3c** with M^{pro} were notably greater than those of **1a**, as confirmed by the molecular docking study. These interactions substantially impact binding affinity, making them vital in the rational development and refinement of drug candidates. These findings provide vital information regarding the specific molecular interactions that play a role in the binding of ensitrelvir, **1a**, and **3c** to M^{pro}, thereby revealing the potential of those compounds as inhibitors of SARS-CoV-2.

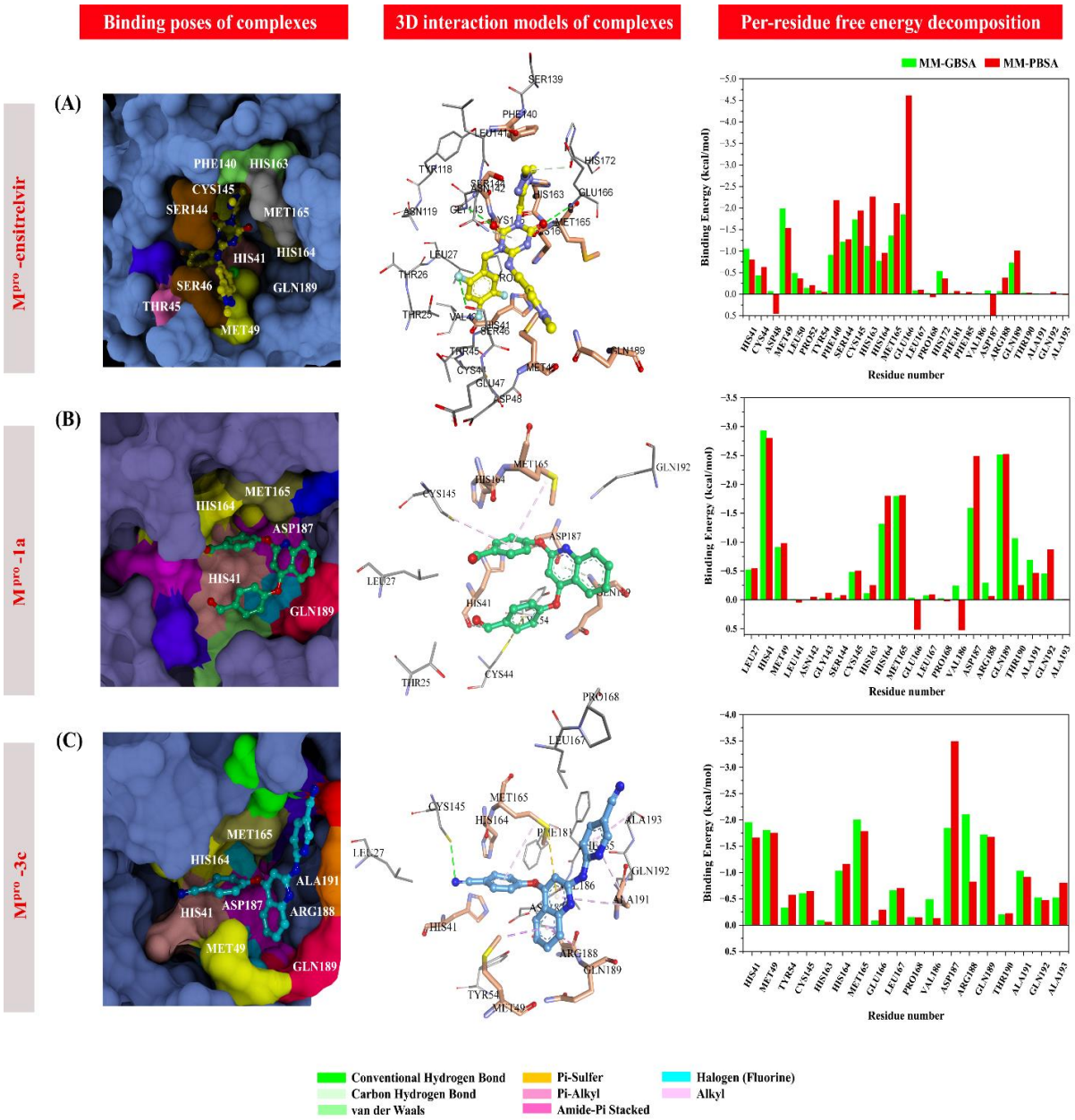

Figure 6 The energy decomposition between the ligands (ensitrelvir, **1a**, and **3c**) and M^{pro}.

SARS-CoV-2 main protease inhibitor screening assay

The inhibitory activity of the selected compounds (**1a** and **3c**) against the SARS-CoV-2 main protease (M^{pro}) was evaluated using the SARS-CoV-2 main protease inhibitor screening assay kit [49]. The inhibitory effects of these compounds are illustrated in Table 3 and Figure 7. Compound **3c** demonstrated excellent inhibitory activity against M^{pro}, with a half-maximal inhibitory concentration (IC_{50}) value of 2.71 μM. While, compound **1a** expected antiviral activity at concentrations value above 50 μM. A positive control in this experiment, namely GC-376, is a M^{pro} inhibitor that blocks the cleavage and activation of essential proteins in viral replication [14-16]. These M^{pro} screening assay data are consistent with our virucidal activity testing and computational approaches, suggesting that **1a** and **3c** also possess significant viral inhibitory potential. Especially, **3c** demonstrated strong binding

efficiency at the catalytic dyad within the M^{pro} active site and exhibited potent inhibitory activity against SARS-CoV-2.

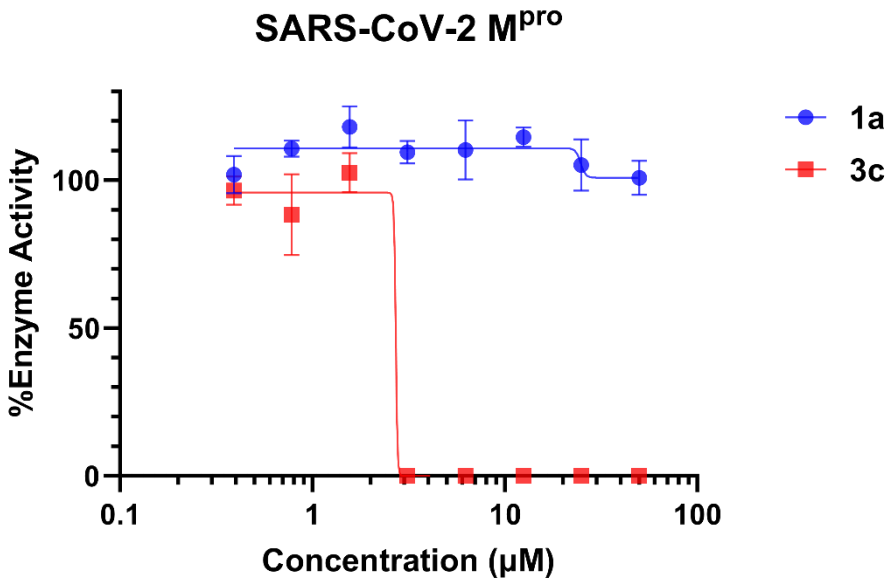

Figure 7 Dose-dependent curve of **1a** and **3c** against SARS-CoV-2 M^{pro}

Table 3 Inhibitory analysis of **1a** and **3c** against SARS-CoV-2 M^{pro}.

Compounds	**SARS-CoV-2 M^{pro}**	
	% Inhibition at 50 μM	**IC_{50} (μM)**
1a	-0.84±4.72	>50
3c	100.00	2.71
GC-376 (+)	69.99±6.96	ND

Results are expressed as the mean ± standard error of inhibitory activity (%). ND is not determined.

Conclusion

In conclusion, this study extensively examined the binding interactions between 2,4-disubstituted quinoline derivatives **1-3(a-d)** and four commercially available medications (ritonavir, ensitrelvir, nirmatrelvir, and paxlovid) with SARS-CoV-2. The research included cytotoxic activity assays, virucidal activity testing, molecular docking, and molecular dynamics simulations of these compounds. According to the cytotoxicity tests, it was determined that **1-3(a-d)** do not cause any harm to Vero E6 cells. The observation was done within a concentration range of 500 to 31.25 μg/mL. The study on the virucidal activity against the SARS-CoV-2 virus of **1-3(a-d)** revealed that all the tested quinolines exhibited significant log reduction values over 2.68, indicating an efficacy of over 99.77% across the tested concentration ranges. Remarkably, quinoline **3c** exhibited the largest log decrease value among the other quinolines tested at the same concentration, showing a similar level of effectiveness as commercially available medications such as ensitrelvir, ritonavir, nirmatrelvir, and paxlovid, which are known for their

potent activity against SARS-CoV-2. Through molecular docking analysis, it was discovered that there are hydrogen bonding and π-sulfur interactions occurring within the pocket of the SARS-CoV-2 main protease (M^{pro}), which plays a crucial role in the viral replication process. Molecular dynamics simulations confirmed the stable binding of ensitrelvir, **1a**, and **3c** with M^{pro}. This was supported by MM-GBSA and MM-PBSA calculations. The binding free energy of M^{pro}-ensitrelvir and M^{pro}-**3c** was determined to be more potent compared to M^{pro}-**1a**. To validate our computational results, we conducted a SARS-CoV-2 main protease (M^{pro}) inhibitor screening assay. The results revealed that **3c** displays strong inhibitory activity against M^{pro}, with IC_{50} value of 2.71 μM. These findings align with our virucidal assays and computational approaches, further confirming **3c** as a potent M^{pro} inhibitor. This study highlights the significant potential of 2,4-disubstituted quinoline derivatives, particularly **3c**, as promising candidates for SARS-CoV-2 inhibition, providing a foundation for the development of effective antiviral agents.

Acknowledgements

The authors are grateful to the Chulabhorn Research Institute and Thailand Science Research and Innovation (TSRI) for financial support (Grant No. 49896/4759817 and 36824/4274395) and Mahidol University (fundamental fund, fiscal year 2024, provided by the National Research Council of Thailand (NSRF)) during this study.

References

1. World Health Organization, WHO COVID-19 dashboard. Available from: https://data.who.int/dashboards/ covid19/deaths?n=c. (Accessed on 11 March 2024).
2. Cui J, Li F, Shi ZL. Origin and evolution of pathogenic coronaviruses. Nat Rev Microbiol. 2019;17:181-92.
3. Shereen MA, Khan S, Kazmi A, Bashir N, Siddique R. COVID-19 infection: origin, transmission, and characteristics of human coronaviruses. J Adv Res. 2020;24:91-8.
4. Cannalire R, Cerchia C, Beccari AR, Di Leva FS, Summa V. Targeting SARS-CoV-2 proteases and polymerase for COVID-19 treatment: state of the art and future opportunities. J Med Chem. 2022;65:2716-46.
5. Gil C, Ginex T, Maestro I, Nozal V, Barrado-Gil L, Cuesta-Geijo MÁ, et al. COVID-19: drug targets and potential treatments. J Med Chem. 2020;63:12359-86.
6. Ullrich S, Nitsche C. The SARS-CoV-2 main protease as drug target. Bioorg Med Chem Lett. 2020;30:127377.
7. Jin Z, Du X, Xu Y, Deng Y, Liu M, Zhao Y, et al. Structure of M^{pro} from SARS-CoV-2 and discovery of its inhibitors. Nature. 2020;582:289-93.
8. Kneller DW, Phillips G, O'Neill HM, Jedrzejczak R, Stols L, Langan P, et al. Structural plasticity of SARS-CoV-2 3CL M^{pro} active site cavity revealed by room temperature X-ray crystallography. Nat Commun. 2020;11:3202.

9. Oerlemans R, Ruiz-Moreno AJ, Cong Y, Kumar ND, Velasco-Velazquez MA, Neochoritis CG, et al. Repurposing the HCV NS3–4A protease drug boceprevir as COVID-19 therapeutics. RSC Med Chem. 2021;12:370-9.
10. Antonopoulou I, Sapountzaki E, Rova U, Christakopoulos P. Inhibition of the main protease of SARS-CoV-2 (M^{pro}) by repurposing/designing drug-like substances and utilizing nature's toolbox of bioactive compounds. Comput Struct Biotechnol J. 2022;20:1306-44.
11. Zagórska A, Czopek A, Fryc M, Jończyk J. Inhibitors of SARS-CoV-2 Main protease (Mpro) as anti-coronavirus agents. Biomolecules. 2024;14:797.
12. Foo CS, Abdelnabi R, Kaptein SJF, Zhang X, Ter Horst S, Mols R, et al. HIV protease inhibitors Nelfinavir and Lopinavir/Ritonavir markedly improve lung pathology in SARS-CoV-2-infected Syrian hamsters despite lack of an antiviral effect. Antiviral Res. 2022;202:105311.
13. Tan B, Joyce R, Tan H, Hu Y, Wang J. SARS-CoV-2 main protease drug design, assay development, and drug resistance studies. Acc Chem Res. 2023;56;157-68.
14. Arafet K, Serrano-Aparicio N, Lodola A, Mulholland AJ, González FV, Świderek K, et al. Mechanism of inhibition of SARS-CoV-2 M^{pro} by N3 peptidyl Michael acceptor explained by QM/MM simulations and design of new derivatives with tunable chemical reactivity. Chem Sci. 2020;27:1433-44.
15. Lin C, Zhu Z, Jiang, H, Zou X, Zeng X, Wang, J, et al. Structural basis for coronaviral main proteases inhibition by the 3CLpro inhibitor GC376. J Mol Biol. 2024;15:168474.
16. Klacsová M, Čelková A, Búcsi A, Martínez JC, Uhríková D. Interaction of GC376, a SARS-COV-2 MPRO inhibitor, with model lipid membranes. Colloids Surf B Biointerfaces. 2022;220:112918.
17. Yamato M, Kinoshita M, Miyazawa S, Seki M, Mizuno T, Sonoyama T. Ensitrelvir in patients with SARS-CoV-2: a retrospective chart review. J Infect Chemother. 2024;30:946-50.
18. Ullrich S, Ekanayake KB, Otting G, Nitsche C. Main protease mutants of SARS-CoV-2 variants remain susceptible to nirmatrelvir. Bioorg Med Chem Lett. 2022;15:128629.
19. Gao K, Wang R, Chen J, Tepe JJ, Huang F, Wei GW. Perspectives on SARS-CoV-2 main protease inhibitors. J Med Chem. 2021;9:16922-55.
20. Pang X, Xu W, Liu Y, Li H, Chen L. The research progress of SARS-CoV-2 main protease inhibitors from 2020 to 2022. Eur J Med Chem. 2023;5:115491.
21. Janin YL. On the origins of SARS-CoV-2 main protease inhibitors. RSC Med Chem. 2023;13:81-118.
22. Noske GD, de Souza Silva E, de Godoy MO, Dolci I, Fernandes RS, Guido RVC, et al. Structural basis of nirmatrelvir and ensitrelvir activity against naturally occurring polymorphisms of the SARS-CoV-2 main protease. J Biol Chem. 2023;299:103004.
23. Hashemian SMR, Sheida A, Taghizadieh M, Memar MY, Hamblin MR, Baghi HB, et al. Paxlovid (Nirmatrelvir/Ritonavir): a new approach to Covid-19 therapy? Biomed Pharmacother. 2023;162:114367.

24. Makarasen A, Patnin S, Vijitphan P, Reukngam N, Khlaychan P, Kuno M, et al. Structural basis of 2-phenylamino-4-phenoxyquinoline derivatives as potent HIV-1 non-nucleoside reverse transcriptase inhibitors. Molecules. 2022;27:461.
25. Techasakul S, Makarasen A, Reuk-ngam N, Khlaychan P, Kuno M, Hannongbua S. Derivatives and composition of quinoline and naphthyridine. WO Patent 2019045655A1, filed 29 August 2017, and issued 7 March 2019.
26. Ngueanngam N, Jityuti B, Patnin S, Boonsri P, Makarasen A, Buranaprapuk A. Multiple spectroscopic and computational studies on binding interaction of 2-phenylamino-4-phenoxyquinoline derivatives with bovine serum albumin. Spectrochim Acta Part A: Mol Biomol Spectrosc. 2024;310:123948.
27. Patnin S, Makarasen A, Vijitphan P, Baicharoen A, Chaivisuthangkura A, Kuno M, et al. Computational screening of phenylamino-phenoxy-quinoline derivatives against the main protease of SARS-CoV-2 using molecular docking and the ONIOM method. Molecules. 2022;27:1793.
28. Patnin S, Makarasen A, Vijitphan P, Baicharoen A, Sirithana W, Techasakul S. Cross-docking and molecular dynamic studies to achieve the potent antiviral HIV-1 nonnucleoside reverse transcriptase inhibitors. Sci Ess J. 2023;39(2):23-37.
29. Creative Biogene Biotechnology, Viral titering-TCID50 assay protocol. Available from: https://www.creative-biogene.com/support/Viral-Titering-TCID50-Assay-Protocol.html (Accessed on 5 December 2023).
30. Barrett PN, Mundt W, Kistner O, Howard MK. Vero cell platform in vaccine production: moving towards cell culture-based viral vaccines. Expert Rev Vaccines. 2009;8:607-18.
31. Reed LJ, Muench H. A simple method of estimating fifty percent endpoints. Am J Epidemiol. 1938;27:493-7.
32. Ghasemi M, Turnbull T, Sebastian S, Kempson I. The MTT assay: utility, limitations, pitfalls, and interpretation in bulk and single-cell analysis. Int J Mol Sci. 2021;22:12827.
33. Phelan K, May KM. Basic techniques in mammalian cell tissue culture. Curr Protoc Cell Biol. 2015;66:1.1.1-22.
34. Bullen CK, Davis SL, Looney MM. Quantification of infectious SARS-CoV-2 by the 50% tissue culture infectious dose endpoint dilution assay. Methods Mol Biol. 2022;2452:131-46.
35. American Society for Testing and Materials (ASTM), ASTM E1053 - Standard to assess virucidal activity of chemicals intended for disinfection of inanimate and nonporous environmental surfaces. Available from: https://microbe-investigations.com/astm-e1053. (Accessed 5 December 2023).
36. Frisch MJ, Trucks GW, Schlegel HB, Scuseria GE, Robb MA, Cheeseman JR, et al. Gaussian 16, Revision, B.01, Gaussian Inc.: Connecticut, United States, 2016.
37. Ngueanngam N, Jityuti B, Patnin S, Makarasen A, Chotiwit S, Samosorn S, et al. In silico investigation of estrogen receptor alpha inhibition by alkyleneoxyberberine derivatives. Sci Ess J. 2025;41:51-64.

38. Zhao Y, Fang C, Zhang Q, Zhang R, Zhao X, Duan Y, et al. Crystal structure of SARS-CoV-2 main protease in complex with protease inhibitor PF-07321332. Protein Cell. 2022;13:689-93.
39. Morris GM, Huey R, Lindstrom W, Sanner MF, Belew RK, Goodsell DS, et al. AutoDock4 and AutoDockTools4: automated docking with selective receptor flexibility. J Comput Chem. 2009;30:2785-91.
40. Abraham MJ, Murtola T, Schulz R, Páll S, Smith JC, Hess B, et al. GROMACS: high performance molecular simulations through multi-level parallelism from laptops to supercomputers. SoftwareX. 2015;1-2:19-25.
41. Case DA, Aktulga HM, Belfon K, Cerutti DS, Cisneros GA, Cruzeiro VWD, et al. AmberTools. J Chem Inf Model. 2023;63:6183-91.
42. Khamto N, Utama K, Boontawee P, Janthong A, Tatieng S, Arthan S, et al. Inhibitory activity of flavonoid scaffolds on SARS-CoV-2 3CLpro: insights from the computational and experimental investigations. J Chem Inf Model. 202464(3):874-91.
43. Maier JA, Martinez C, Kasavajhala K, Wickstrom L, Hauser KE, Simmerling C. ff14SB: improving the accuracy of protein side chain and backbone parameters from ff99SB. J Chem Theory Comput. 2015; 11:3696-713.
44. Mark P, Nilsson L. Structure and dynamics of the TIP3P, SPC, and SPC/E water models at 298 K. J Phys Chem A. 2001;105:9954–60.
45. Humphrey W, Dalke A, Schulten K. VMD: visual molecular dynamics. J Mol Graph. 1996;14:33-8.
46. Virtanen SI, Niinivehmas SP, Pentikäinen OT. Case-specific performance of MM-PBSA, MM-GBSA, and SIE in virtual screening. J Mol Graph Model. 2015;62:303-18.
47. Altharawi A. Targeting toxoplasma gondii ME49 TgAPN2: a bioinformatics approach for antiparasitic drug discovery. Molecules. 2023;28:3186.
48. Sahakyan H. Improving virtual screening results with MM/GBSA and MM/PBSA rescoring. J Comput Aided Mol Des. 2021;35:731-6.
49. Cayman Chemical. SARS-CoV-2 main protease inhibitor screening assay kit. Available from: https://www.caymanchem.com/product/701960/sars-cov-2-main-protease-inhibitor-screening-assay-kit. (Accessed 18 February 2025).
50. International Organization for Standardization. 10993-5:2009, Biological evaluation of medical devices-part 5: tests for in vitro cytotoxicity, 3rd ed. 2009.
51. Microchem Laboratory. Log and percent reductions in microbiology and antimicrobial testing. Available from: https://microchemlab.com/information/log-and-percent-reductions-microbiology-and-antimicrobial-testing. (Accessed 5 December 2023).
52. Khamto N, Utama K, Tateing S, Sangthong P, Rithchumpon P, Cheechana N, et al. Discovery of natural bisbenzylisoquinoline analogs from the library of thai traditional plants as SARS-CoV-2 3CLPro inhibitors: in silico molecular docking, molecular dynamics, and in vitro enzymatic activity. J Chem Inf Model. 2023;63:2104-21.

53. Vuong W, Khan MB, Fischer C, Arutyunova E, Lamer T, Shields J, et al. Feline coronavirus drug inhibits the main protease of SARS-CoV-2 and blocks virus replication. J Nat Commun. 2020;11:4282.
54. Wang H, Pei R, Li X, Deng W, Xing S, Zhang Y, et al. The structure-based design of peptidomimetic inhibitors against SARS-CoV-2 3C like protease as Potent anti-viral drug candidate. Eur J Med Chem. 2022;238:114458.
55. Cheng S-C, Chang G-G, Chou C-Y. Mutation of Glu-166 blocks the substrate-induced dimerization of SARS coronavirus main protease. Biophys J. 2010;98:1327-36.
56. Sahoo M, Behera DU, Gaur M, Subudhi E. Molecular docking, molecular dynamics simulation, and MM/PBSA analysis of ginger phytocompounds as a potential inhibitor of AcrB for treating multidrug-resistant *Klebsiella pneumoniae* infections. J Biomol Struct Dyn. 2025;43(1):3585-601.
57. Halim SA, Waqas M, Asim A, Khan M, Khan A, Al-Harrasi A. Discovering novel inhibitors of P2Y12 receptor using structure-based virtual screening, molecular dynamics simulation and MMPBSA approaches. Comput Biol Med. 2022;147:105743.
58. Rafique A, Muhammad S, Iqbal J, Al-Sehemi AG, Alshahrani MY, Ayub K, et al. Exploring the inhibitory potential of novel piperidine-derivatives against main protease (Mpro) of SARS-CoV-2: a hybrid approach consisting of molecular docking, MD simulations and MMPBSA analysis J Mol Liq. 2023;382:121904.
59. Khan MT, Ali S, Zeb MT, Kaushik AC, Malik SI, Wei D-Q. Gibbs free energy calculation of mutation in PncA and RpsA associated with pyrazinamide resistance. Front Mol Biosci. 2020;7:52.
60. Valdés-Tresanco MS, Valdés-Tresanco ME, Valiente PA, Moreno E. gmx_MMPBSA: a new tool to perform end-state free energy calculations with GROMACS. J Chem Theory Comput. 2021;17:6281-91.
61. Wang E, Sun H, Wang J, Wang Z, Liu H, Zhang JZH, et al. End-point binding free energy calculation with MM/PBSA and MM/GBSA: strategies and applications in drug design. Chem Rev. 2019;119:9478-508.